

Appendix A: Vegetation Classification and DEM Co-registration

1. Introduction

Advancements in remote sensing and photogrammetry have significantly improved our ability to quantify large-scale geomorphic changes. Techniques such as Light Detection and Ranging (LiDAR) and Structure from Motion (SfM) offer unprecedented spatial resolution and data coverage, enabling the detection of subtle geomorphic alterations over broad areas (Ellet et al., 2019; East et al., 2021). However, SfM and LiDAR products usually have some degree of misalignment that introduces error when attempting to perform geomorphic change detection analyses on these elevation datasets (Chirico et al., 2020; Hugonnet et al., 2021; Niculiță et al., 2020). Although iterative closest point (ICP) algorithms effectively co-register point clouds prior to DEM creation, these methods demand good initial alignment, are sensitive to outliers, and become computationally intensive with large or high-resolution datasets (Cucchiaro et al., 2020). Alternatively, a DEM co-registration algorithm described by Nuth and Kaab (2011) has demonstrated success in aligning LiDAR datasets in glacial mass balance studies but remains underexplored for co-registering SfM DSMs and LiDAR DEMs in a geomorphic context.

This paper proposes a novel workflow designed to address this gap by masking vegetation from SfM-derived DSMs before co-registration with airborne LiDAR-derived DEMs. The proposed methodology is demonstrated through aligning pre-fire LiDAR DEMs with post-fire SfM DSMs, facilitating subsequent analyses of geomorphic change to better understand the drivers of hillslope erosion following wildfire.

Methods

2.1 Site Description

The ETF study area includes three tributary study areas, including two lower elevation areas (ETF-LM2, ETF-LPM), one middle elevation area (ETF-MM), with elevations ranging from 2,559 to 3,495 m. In the ETF study areas, access constraints due to extreme topography and flash flooding restricted flights to lower watershed areas, which ranged in size from 0.61 to 1.44 km². All study areas drain directly into Willow Creek. A sizeable debris flow occurred in ETF-LPM before the fire, which deposited a large deposit of unconsolidated sediment in the channel corridor. Burn severity across the ETF sites was largely moderate to high, resulting in substantial vegetation loss and ground debris. ETF sites fall within sedimentary mid-elevation and subalpine forest ecoregions, with dominant vegetation including lodgepole pine, grouse whortleberry, subalpine fir, Engelmann spruce, russet buffaloberry, and diverse shrub and grass groundcovers (Chapman et al., 2006; NRCS, 2021). Geologic substrate primarily includes sandstone-based Frisco, Howlett, and Scout family moist complexes (NRCS, 2021). Annual precipitation is highly variable, predominantly as winter snowfall and intense localized convective summer storms.

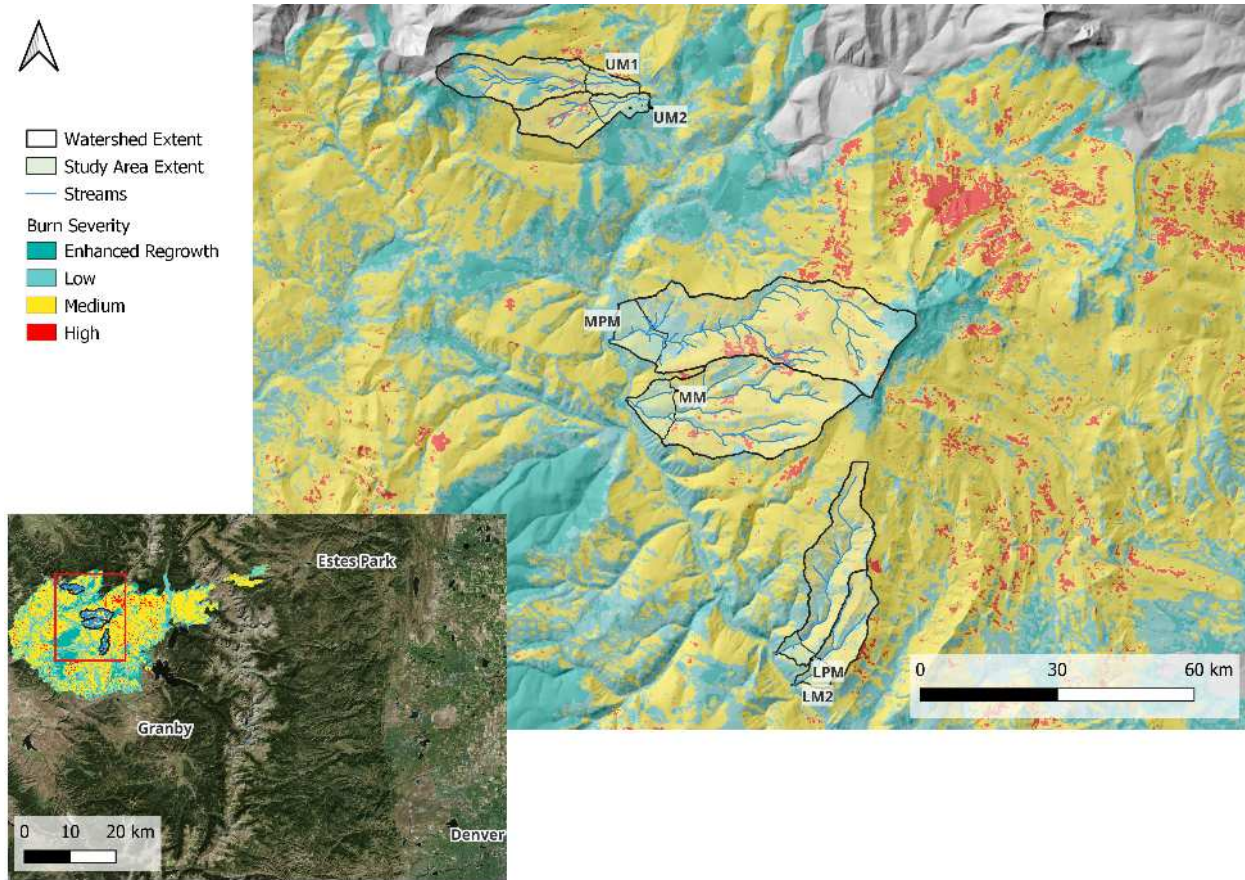


Figure 1: Map of the East Troublesome burn scar, soil burn severity map, and study watersheds.

All study areas have a semi-arid climate, with annual precipitation ranging from 400 mm to 500 mm, primarily from winter snow and summer convective thunderstorms (PRISM Climate Group, n.d.). Burn severity across the study areas was largely low to moderate, resulting in substantial vegetation loss and ground debris. Vegetation cover, mean slope, and burn severity were assessed using pre-fire LiDAR DEMs, BAER maps, and RGB orthomosaics (Table 1).

| Burn Scar | Study Site | Study Area (km ²) | Basin Area (km ²) | Elevation Min (m) | Elevation Max (m) | Slope Mean (degrees) | 10-min Storm Accumulation Mean (mm) | dNBR Mean | NDVI Mean |
|-----------|------------|-------------------------------|-------------------------------|-------------------|-------------------|----------------------|-------------------------------------|-----------|-----------|
| ETF | LM2 | 0.61 | 2.23 | 2560 | 3010 | 17.5 | 218.8 | 425.8 | 0.38 |
| | LPM | 0.65 | 4.46 | 2559 | 3330 | 21.4 | 264.1 | 418.8 | 0.39 |
| | MM | 1.14 | 9.18 | 2625 | 3495 | 16.7 | 318.2 | 555.6 | 0.37 |

Table 1: Summary of watershed and fire metrics for each data collection area

2.2 Data Collection

ETF surveys were collected using the WingtraOne Gen II fixed-wing (Wingtra) drone, which can be pre-programmed to collect surveys autonomously. The Wingtra drone is equipped with a 42MP Sony RX1R II camera and was programmed to fly at 120 m above ground level (relative to the USGS 1/3 arc-second Digital Elevation Model) with a 70% side and front photo overlap, corresponding to a ground sampling distance (GSD) of 1.6 cm per pixel.

A Topcon GR-5 GNSS base station unit receiver was used for this study for communications with the RTK GNSS modules on board the Wingtra. The receiver was set up no more than 1 km from the take-off location for the drone and collected static data at 1-second intervals for at least one hour including during the flight. Static positioning data from the base station were corrected with NOAA's Online Positioning User Service (OPUS), which references observations to the National Spatial Reference System (NSRS) with typical accuracies of a few centimeters, depending on site conditions and occupation duration. The Wingtra is equipped with an onboard high-precision post processed kinematic (PPK) global navigation satellite system (GNSS) module, which meant it was not necessary to use ground control points (GCPs) to georeference images during post-processing (de Haas et al., 2021). All surveys were flown in early July 2023 and OPUS corrected, PPK processed images had vertical and horizontal errors that ranged from <1 to 5 cm.

The images were processed using Agisoft Metashape with a structure-from-motion (SfM) workflow to generate dense point clouds, digital elevation models (DEMs), and orthomosaics for each flight. SfM enables the reconstruction of 3D topography from overlapping 2D images with location data. To provide a common resolution for equal comparison across watersheds, DEMs were all exported at a resolution of 6 cm, and orthomosaics were exported at a resolution of 2 cm.

LiDAR DEMs were obtained from OpenTopography and had a resolution of 1 meter. The USGS 2020 LiDAR DEM (USGS, 2022a) was flown over the ETF study sites between September and October 2020, immediately prior to East Troublesome fire.

2.3 Vegetation Classification

The vegetation in the SfM DSMs was then classified and masked to create a DEM using a XGBoost classifier, which is a variant of a gradient boosting random forest classifier. The input layers to the XGBoost land cover classifier include a roughness raster created from the DSM and the red, green and blue bands of the orthomosaic image. The inputs also included an Excessive Green Index (ExGI) band:

$$\text{ExGI} = 2 \cdot G - (R + B) \quad (1)$$

where R, G, and B are the red, green, and blue components of the orthomosaic image, respectively, and a saturation band:

$$\text{Saturation} = 1 - \min([R, G, B]) \quad (2)$$

where $\min(R, G, B)$ are the minimum values of the red, green, and blue components for each pixel across the image data.

After performing a sensitivity analysis on the spatial resolution of the input raster, it was determined that the input layers could be downsampled from their 2-centimeter native resolution to a 5-centimeter resolution without sacrificing performance. The classification model was trained using the downsampled input layers and shapefiles labeled with three classes of vegetation (shrubs/grasses, logs/trees, and burned logs/trees), two classes of bare (light and dark colored bare earth), and one class of water. A separate validation set of shapefiles was additionally created, and a confusion matrix was used for accuracy assessment. To enhance model performance, a sieving function was applied to filter out small, isolated patches of bare earth less than 100 cm² that were likely classification artifacts.

2.4 DEM Co-registration

The DEM co-registration was performed using a Python implementation of the Nuth and Kääb (2011) algorithm as implemented by Shean et al. (2016). This method corrects three primary bias types—horizontal misalignment, elevation-dependent offset, and acquisition-geometry effects—by iteratively translating the SfM DEM to minimize elevation error relative to the LiDAR DEM. Corrections are driven by slope- and aspect-weighted difference metrics: at each iteration, the algorithm computes translation vectors that reduce systematic elevation discrepancies, repeating until shifts fall below a convergence threshold of 1 cm. Prior to coregistration, both DEMs were resampled to a common 20 cm grid spacing, a resolution selected through a sensitivity analysis that yielded the lowest co-registration error. This approach ensures that residual biases in the co-registered DEMs are minimized, thereby improving the reliability of subsequent elevation-change estimates.

2.5 Geomorphic Change Quantification

The original, co-registered, and vegetation-masked, co-registered DEMs were each differenced with the LiDAR dataset to create three DEMs of Difference (DoD) for each study area. When quantifying geomorphic change uncertainty must be accounted for in DoD analyses to determine whether observed changes are statistically significant (Brasington et al., 2003; Lane et al., 2003). When dealing with gross erosion and deposition, changes smaller than a defined ‘level of detection’ (LoD) are typically excluded from further analysis to avoid misinterpreting measurement noise as genuine change.

Random vertical error was quantified by extracting precision point estimates directly from Metashape using a Python script, followed by interpolation using kriging to produce an uncertainty raster (James et al., 2017). To propagate these random errors into the DoD at a 95% confidence interval, elevation differences between surveys were assumed to follow an independent Gaussian distribution. Thus, the LoD of each DoD was calculated using the following equation (Anderson, 2018):

$$\delta_{\text{DoD}_{i,j}} = \pm 1.96 \cdot \sqrt{\delta_{\text{LiDAR}}^2 + \delta_{\text{SfM}_{i,j}}^2} \quad (3)$$

where:

- δ_{LiDAR} is the Root Mean Square Error in elevation (RMSE_z) reported for LiDAR data (10 cm).
- $\delta_{SfMi,j}$ is the RMSE_z of the Structure from Motion (SfM) data at grid cell (i, j).

Each resulting LoD raster was subsequently applied to threshold its corresponding DoD, generating an unbiased representation of geomorphic change for the study period.

3. Results

3.1 Vegetation Classification

Precision reflects the reliability of positive predictions: it answers the question “of all the areas the model labels as our target class, how many are actually correct?” In contrast, recall captures completeness: it answers the question “of all the true occurrences in the landscape, how many did the model successfully detect?” A model tuned for high precision will rarely misidentify non-target areas but may overlook subtle or marginal true patches, whereas one optimized for high recall will detect most true occurrences at the risk of including more false positives. The F₁ score balances precision and recall into a single metric, allowing for the balanced weighting of false alarms and missed detections. For a study concerned with quantifying geomorphic change, precision of the bare earth classification is the most important metric, as vegetation falsely classified as bare earth can introduce large vertical errors.

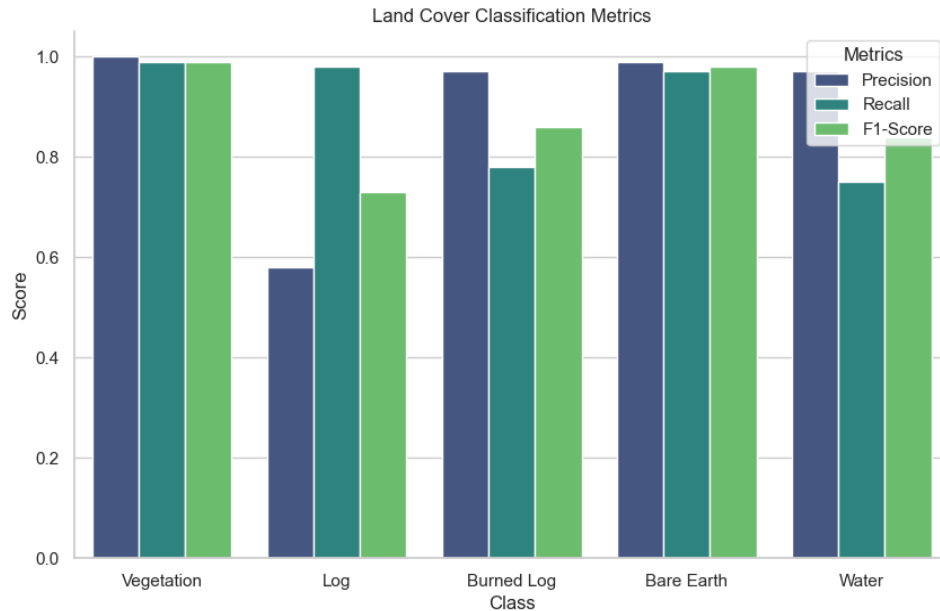


Figure 2: Precision, recall and F1 score performance of the random forest land cover classification algorithm

The random forest vegetation classifier achieved 97.5% precision and 98.5% recall for bare earth classification and 96.7% precision and 97.7% recall for vegetation classification (weighted

average of the three vegetation classes), with the performance of other classes detailed in Figure 3. Logs and water were most commonly mistaken for bare earth (and vice versa), likely due to the relatively similar RGB spectral signature of dark colored logs, water and bare earth.

We can also assess the random forest classifier qualitatively by inspecting the mask in Figure 3. The mask shows excellent delineation in the channel and solid—albeit slightly weaker—performance on the hillslopes.

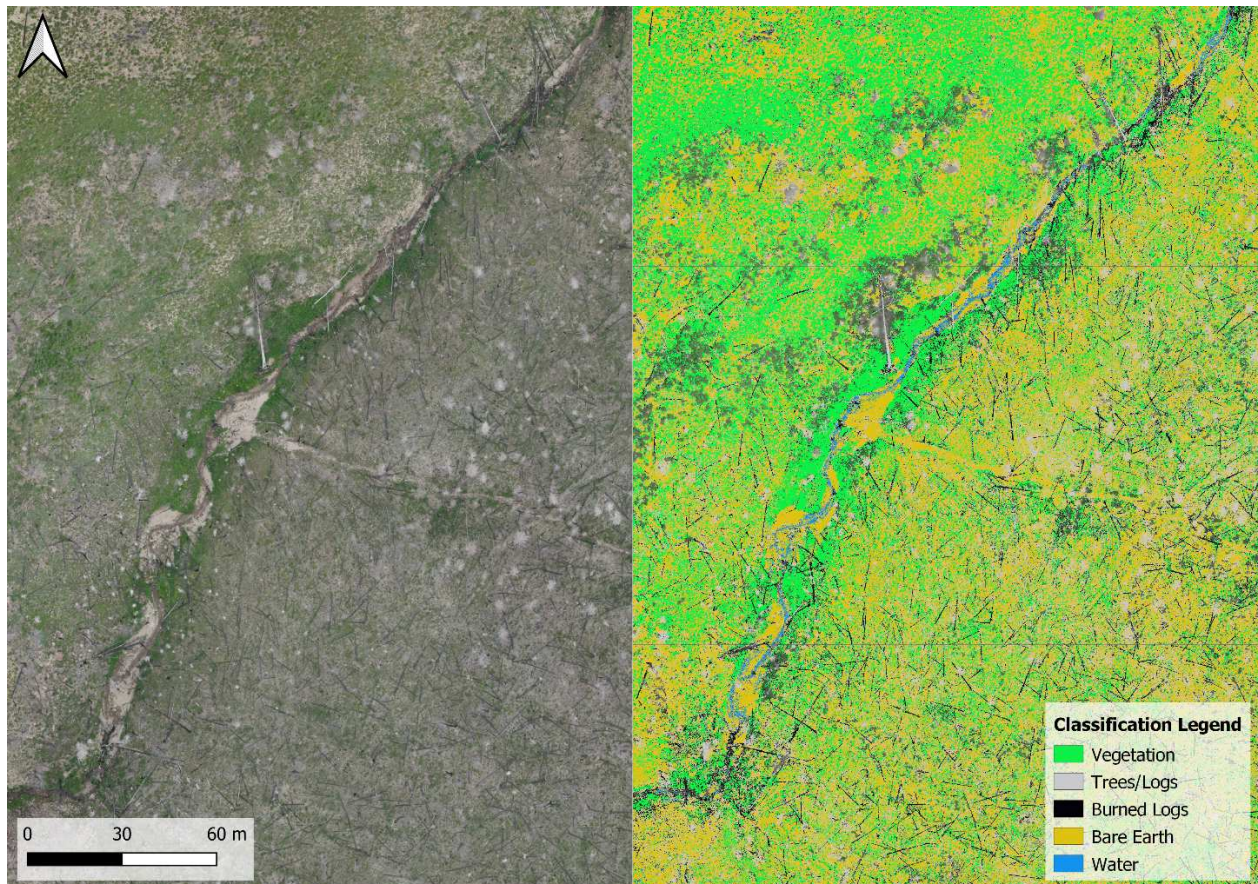


Figure 3: Classified ground cover along a reach in the LM2 watershed.

3.2 DEM Co-Registration

The DoDs produced after vegetation masking and co-registration did not show signs of systematic bias, such as doming, elevation-dependent trends, slope-dependent trends, or consistent vertical offsets. The magnitude of the LoD rasters was dominated by the LiDAR error, with threshold values ranging from 20 – 23 cm.

Figures 4, 5 & 6 illustrate the qualitative improvements achieved through co-registration and vegetation masking in two ETF study areas. Prior to alignment, the original DoDs showed no clear patterns of erosion or deposition, both on hillslopes and within channels. Following co-registration alone, erosion and deposition patterns emerged on hillslopes and within channels,

though residual noise remained evident on hillslopes, and some vegetated areas adjacent to channels were incorrectly classified as deposition. Finally, after applying vegetation masking prior to co-registration, the clearest erosion and deposition patterns became apparent. Features such as rills and gullies on hillslopes could be distinctly resolved and quantitatively analyzed with a significant reduction in noise, although some patches of “erosion” remained on the hillslopes where there were no obvious erosional features observed in the orthomosaic.

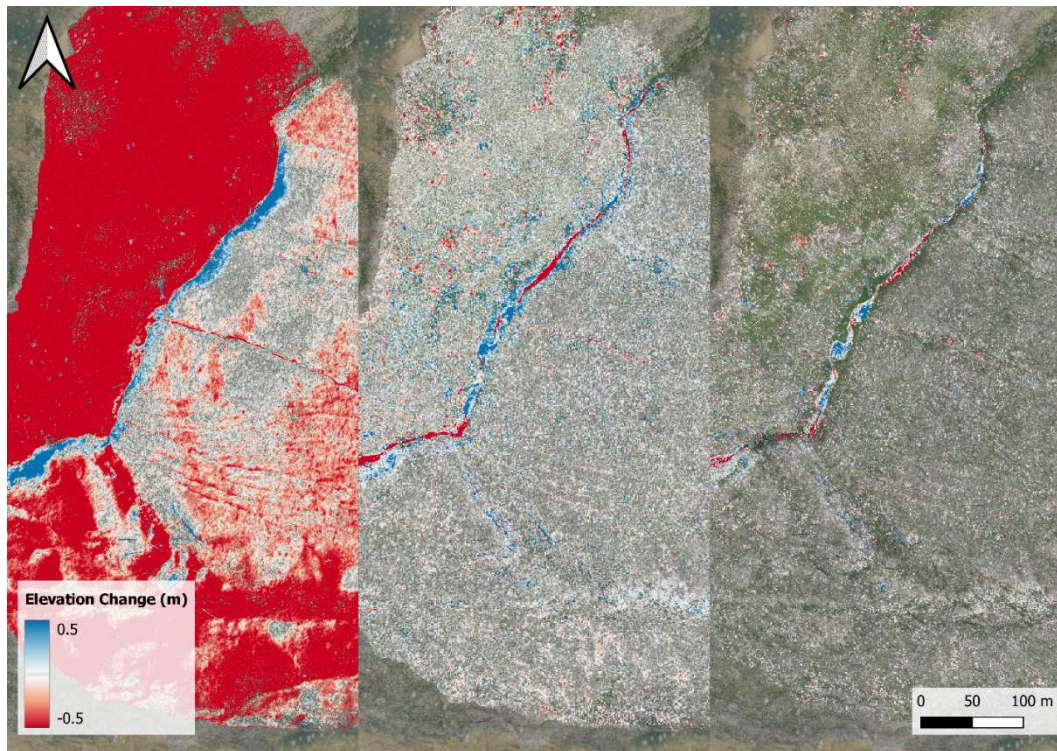


Figure 4: DEM co-registration results for the LM2 watershed. From left to right: (a) original DoD, (b) DoD after co-registration, and (c) vegetation masked, co-registered DoD.

Figure 7 illustrates the influence of vegetation masking prior to co-registration on a relatively stable to depositional section of LM2. Comparison of orthomosaic imagery from 2022 and 2023 indicates minimal geomorphic change in the upstream portion of the reach, while the downstream section is primarily depositional. Erosion volumes derived from the DoDs progressively decrease from the original DoD to the co-registered DoD, with the vegetation masked, co-registered DoD exhibiting the lowest overall measured erosion.

Figure 8 shows the cumulative erosion within each study area. Errors in channel erosion measurement due to poor coregistration propagate when summed over the study area, with the differences in calculated volume 4-10 times greater between the original and vegetation masked, coregistered DEMs.

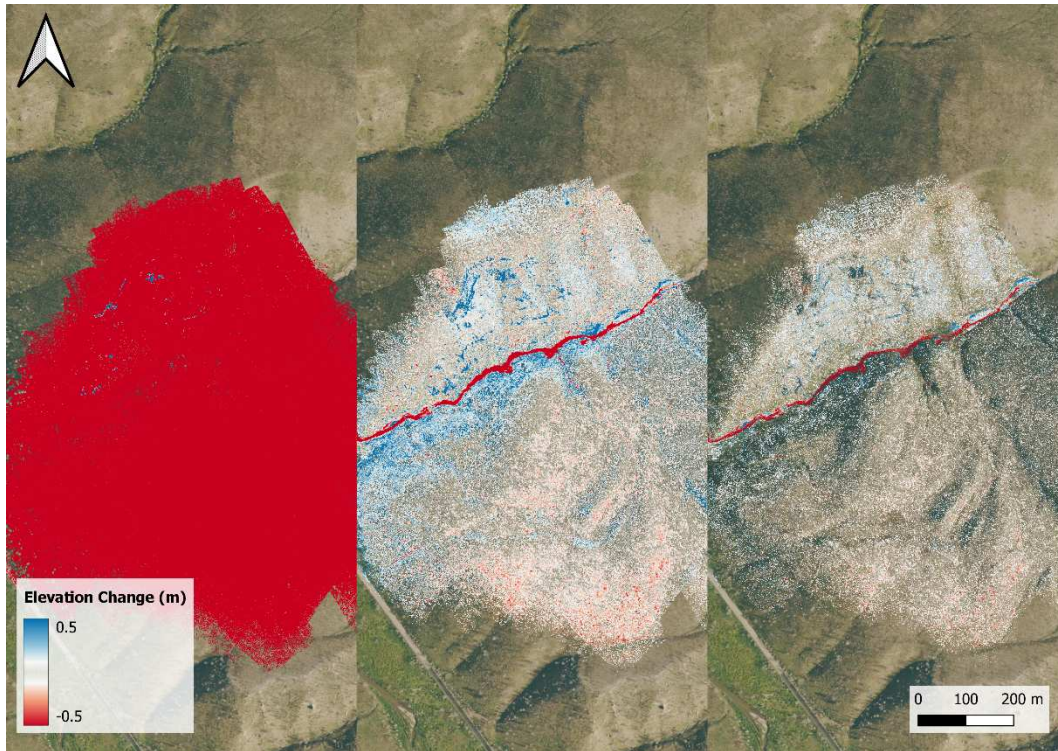


Figure 5: DEM co-registration results for the LPM watershed. From left to right: (a) original DoD, (b) DoD after co-registration, and (c) vegetation masked, co-registered DoD.

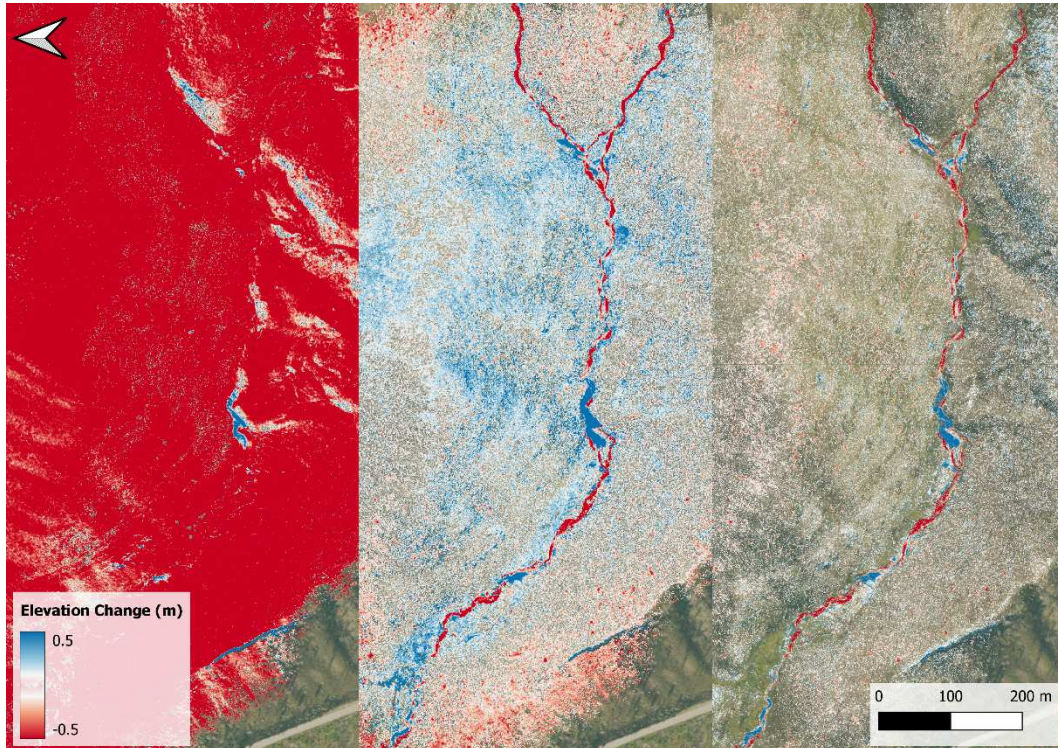


Figure 6: DEM co-registration results for the MM watershed. From left to right: (a) original DoD, (b) DoD after co-registration, and (c) vegetation masked, co-registered DoD.

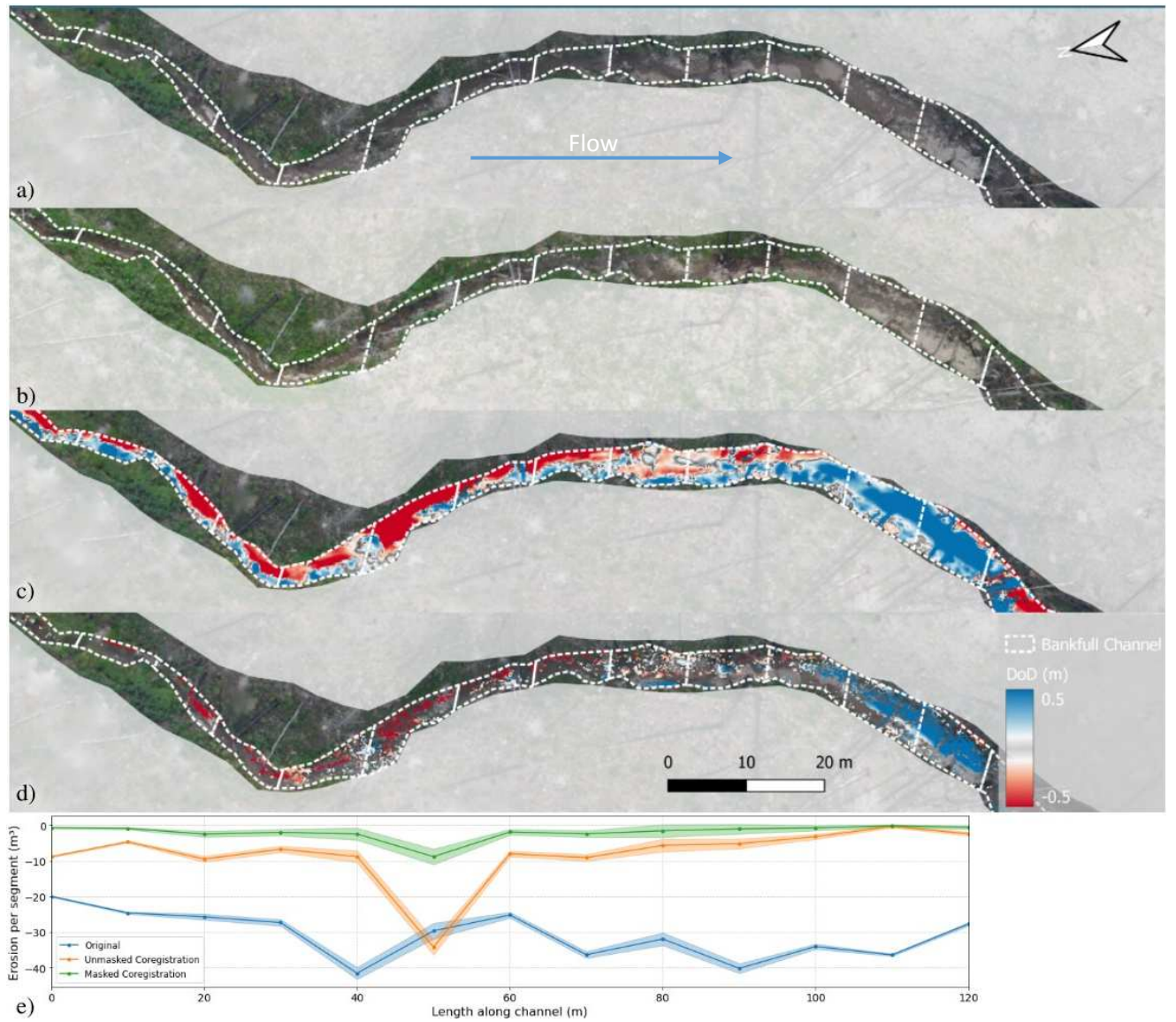


Figure 7. Reach-scale evaluation of co-registration alignment in a stable-depositional stream reach in the upper ETF-LM2 study area (erosion expected ≈ 0). (a) September 2022 orthomosaic; (b) July 2023 orthomosaic; (c) unmasked co-registered DSM difference; (d) vegetation-masked co-registration; (e) volumetric erosion in each segment from the SfM (July 2023) minus LiDAR (September 2020) DoD, with curves shown for the original, unmasked, and vegetation-masked alignments.

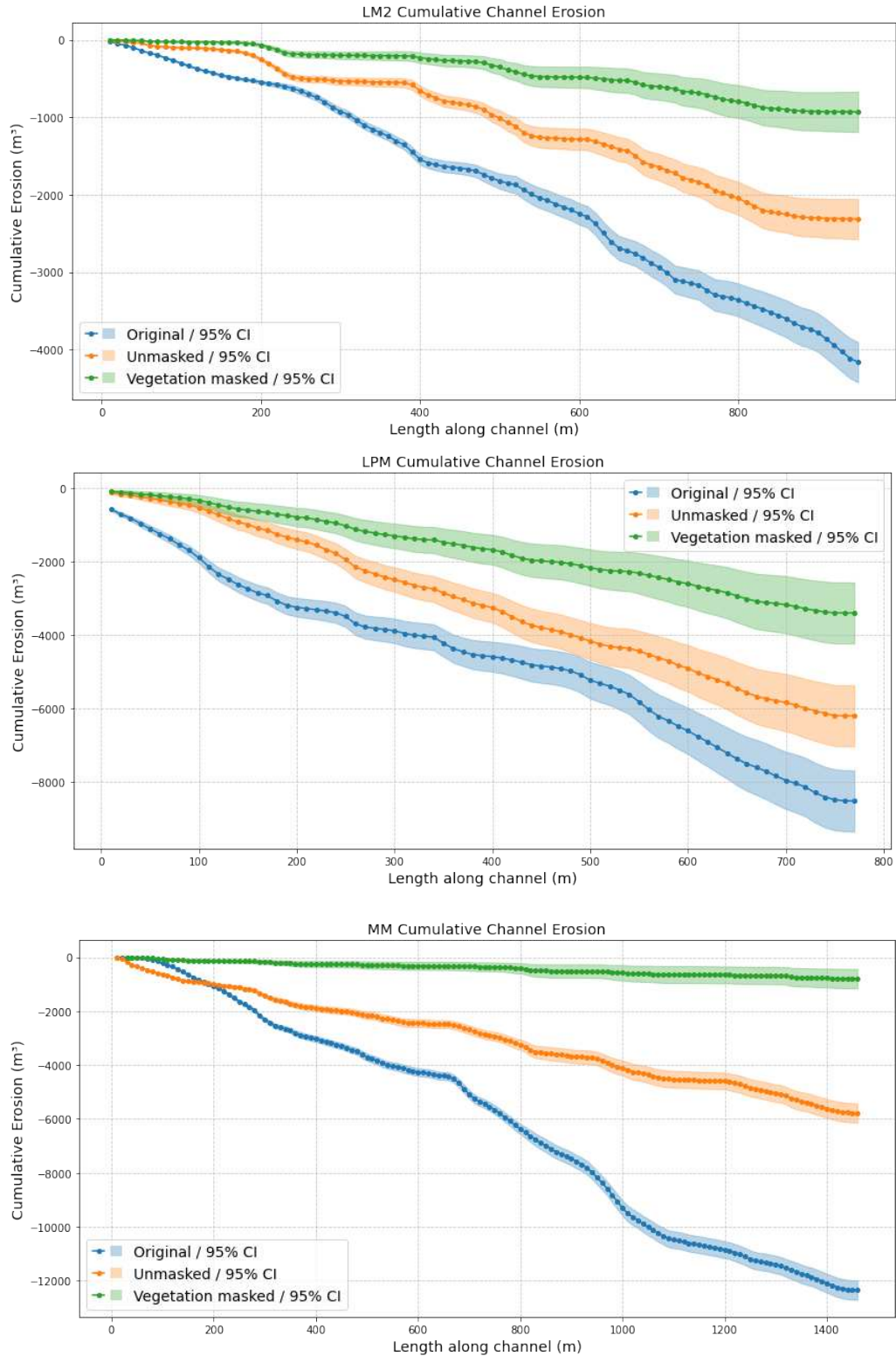


Figure 8. Cumulative erosion ETF study areas, with 0 being the most upstream point in the study area. Error due to vegetation in the SfM DSM and the misalignment of DEMs can cause order of magnitude differences in the calculated erosion in the channel when summed over an entire watershed.

4. Discussion & Conclusion

Vegetation masking prior to DEM co-registration played a critical role in improving the fidelity of geomorphic change detection. The high precision of bare earth classification (97.5%) ensured that vegetated areas were reliably excluded from the SfM DSMs, reducing vertical discrepancies between datasets and mitigating false signals in the DEMs of Difference. This is particularly important in post-fire environments, where vegetation loss is widespread but uneven, and where residual vegetation—particularly logs and dense shrub patches—can create substantial vertical error in SfM surfaces. By minimizing these artifacts, the classifier allowed for more consistent alignment with the LiDAR DEMs, which are typically vegetation-filtered and represent true ground elevation.

The co-registration algorithm itself effectively minimized systematic vertical and horizontal biases, as indicated by the lack of slope- or elevation-dependent residuals in the final DoDs. However, the greatest performance gains were observed when co-registration was paired with vegetation masking. This combined approach resolved noise that persisted even after coregistration alone, particularly on hillslopes and at the channel margins where vegetation-related errors are most pronounced in SfM data. In several cases, the masking procedure revealed fine-scale erosional features such as rills and gullies that were obscured by vegetation-induced elevation noise in the unmasked data.

At the watershed scale, these refinements substantially reduced error in volumetric estimates of erosion and deposition. The results from Figure 8 demonstrate that differences in estimated erosion between unmasked and vegetation-masked workflows can vary by an order of magnitude, with the masked, co-registered workflow consistently producing more conservative and geologically plausible estimates. These discrepancies highlight the importance of both accurate land cover classification and robust co-registration techniques in high-resolution topographic change detection workflows.

In channel corridors, where the majority of sediment transport occurs following wildfire, the improved alignment and surface accuracy enabled by vegetation masking is especially consequential. Misclassification of vegetated channel features as bare earth introduces the potential for significant false erosion signals. The classifier's ability to distinguish between vegetation and true channel bed features reduced these errors, enabling more confident identification of depositional zones and erosion hot spots.

This workflow demonstrates the value of integrating a random forest land cover classification with DEM co-registration to enhance geomorphic change detection in post-fire landscapes. While the co-registration algorithm alone is capable of reducing alignment bias, its effectiveness is significantly augmented by prior vegetation masking. Together, these methods offer a reliable approach for detecting geomorphic change in the channel network across large, heterogeneous watersheds with high-resolution topographic data.

References

- Agisoft Metashape User Manual - Professional Edition, Version 2.0. (2023).
- Anderson, S. (2018). Uncertainty in quantitative analyses of topographic change: Error propagation and the role of thresholding. *Earth Surface Processes and Landforms*, 44. <https://doi.org/10.1002/esp.4551>
- Angileri, S. E., Conoscenti, C., Hochschild, V., Märker, M., Rotigliano, E., & Agnesi, V. (2016). Water erosion susceptibility mapping by applying Stochastic Gradient Treeboost to the Imera Meridionale River Basin (Sicily, Italy). *Geomorphology*, 262, 61–76. <https://doi.org/10.1016/j.geomorph.2016.03.018>
- Benavides-Solorio, J., & MacDonald, L. H. (2001). Post-fire runoff and erosion from simulated rainfall on small plots, Colorado Front Range.
- Chen, A., Zhuang, J., & Han, X. (2022). An Improved ICP Algorithm for 3D Point Cloud Registration. In *2022 3rd International Conference on Pattern Recognition and Machine Learning (PRML)* (pp. 205–210). Chengdu, China: IEEE. <https://doi.org/10.1109/PRML56267.2022.9882220>
- Chirico, P., DeWitt, J., & Bergstresser, S. (2020). Evaluating Elevation Change Thresholds between Structure-from-Motion DEMs Derived from Historical Aerial Photos and 3DEP LiDAR Data. *Remote Sensing*, 12(10), 1625. <https://doi.org/10.3390/rs12101625>
- Cook, K. L. (2017). An evaluation of the effectiveness of low-cost UAVs and structure from motion for geomorphic change detection. *Geomorphology*, 278, 195–208. <https://doi.org/10.1016/j.geomorph.2016.11.009>
- Cucchiaro, S., Maset, E., Cavalli, M., Crema, S., Marchi, L., Beinat, A., & Cazorzi, F. (2020). How does co-registration affect geomorphic change estimates in multi-temporal surveys? *GIScience & Remote Sensing*, 57(5), 611–632. <https://doi.org/10.1080/15481603.2020.1763048>
- East, A. E., Logan, J. B., Dartnell, P., Lieber-Kotz, O., Cavagnaro, D. B., McCoy, S. W., & Lindsay, D. N. (2021). Watershed Sediment Yield Following the 2018 Carr Fire, Whiskeytown National Recreation Area, Northern California. *Earth and Space Science*, 8(9), e2021EA001828. <https://doi.org/10.1029/2021EA001828>
- Ellett, N. G., Pierce, J. L., & Glenn, N. F. (2019). Partitioned by process: Measuring post-fire debrisflow and rill erosion with Structure from Motion photogrammetry.
- Foltz, R. B., & Wagenbrenner, N. S. (2010). An evaluation of three wood shred blends for post-fire erosion control using indoor simulated rain events on small plots. *CATENA*, 80(2), 86–94. <https://doi.org/10.1016/j.catena.2009.09.003>
- Ghorbanzadeh, O., Sansar Raj Meena, Thomas Blaschke, & agannath Aryal. (2019). UAV-Based Slope Failure Detection Using Deep-Learning Convolutional Neural Networks. Retrieved from <https://www.mdpi.com/2072-4292/11/17/2046>
- Hayter, L. (2023). EVALUATING POST-FIRE GEOMORPHIC CHANGE ON PAIRED MULCHED AND UNMULCHED WATERSHEDS USING REPEAT DRONE SURVEYS.
- Hugonnet, R., McNabb, R., Berthier, E., Menounos, B., Nuth, C., Girod, L., et al. (2021). Accelerated global glacier mass loss in the early twenty-first century. *Nature*, 592(7856), 726–731. <https://doi.org/10.1038/s41586-021-03436-z>
- James, M., Stuart Robson, & Mark W. Smith. (2017). 3-D uncertainty-based topographic change detection with structure-from-motion.pdf.
- James, M. R., Antoniazza, G., Robson, S., & Lane, S. N. (2020). Mitigating systematic error in topographic models for geomorphic change detection: accuracy, precision and considerations beyond off-nadir imagery. *Earth Surface Processes and Landforms*, 45(10), 2251–2271. <https://doi.org/10.1002/esp.4878>
- Khosravi, K., Rezaie, F., Cooper, J. R., Kalantari, Z., Abolfathi, S., & Hatamiafkoueih, J. (2023). Soil water erosion susceptibility assessment using deep learning algorithms. *Journal of Hydrology*, 618, 129229. <https://doi.org/10.1016/j.jhydrol.2023.129229>
- Miller, J. D., Safford, H. D., Crimmins, M., & Thode, A. E. (2009). Quantitative Evidence for Increasing Forest Fire Severity in the Sierra Nevada and Southern Cascade Mountains, California and Nevada, USA. *Ecosystems*, 12(1), 16–32. <https://doi.org/10.1007/s10021-008-9201-9>
- Morris, S. E., & Moses, T. A. (1987). Forest Fire and the Natural Soil Erosion Regime in the Colorado Front Range. *Annals of the Association of American Geographers*, 77(2), 245–254. <https://doi.org/10.1111/j.1467-8306.1987.tb00156.x>
- Mosavi, A., Sajedi-Hosseini, F., Choubin, B., Taromideh, F., Rahi, G., & Dineva, A. A. (2020). Susceptibility Mapping of Soil Water Erosion Using Machine Learning Models. *Water*, 12(7), 1995. <https://doi.org/10.3390/w12071995>

- Murray, J. T. (2023). LARGE-SCALE REMOTE SENSING OF GEOMORPHIC CHANGE IN MULCHED AND UNMULCHED WATERSHEDS BURNED IN THE 2020 EAST TROUBLESOME FIRE, COLORADO.
- Niculiță, M., Mărgărint, M. C., & Tarolli, P. (2020). Chapter 10 - Using UAV and LiDAR data for gully geomorphic changes monitoring. In P. Tarolli & S. M. Mudd (Eds.), *Developments in Earth Surface Processes* (Vol. 23, pp. 271–315). Elsevier. <https://doi.org/10.1016/B978-0-444-64177-9.00010-2>
- Nuth, C., & Kääb, A. (2011). Co-registration and bias corrections of satellite elevation data sets for quantifying glacier thickness change. *The Cryosphere*, 5(1), 271–290. <https://doi.org/10.5194/tc-5-271-2011>
- Over, Ritchie, & Kranenburg. (2021). *Processing coastal imagery with Agisoft Metashape Professional Edition, version 1.6—Structure from motion workflow documentation* (Open-File Report).
- Prats, S. A., Wagenbrenner, J. W., Martins, M. A. S., Malvar, M. C., & Keizer, J. J. (2016). Mid-term and scaling effects of forest residue mulching on post-fire runoff and soil erosion. *Science of The Total Environment*, 573, 1242–1254. <https://doi.org/10.1016/j.scitotenv.2016.04.064>
- Robichaud, P. R., Beyers, J. L., & Neary, D. G. (2000). *Evaluating the effectiveness of postfire rehabilitation treatments* (No. RMRS-GTR-63) (p. RMRS-GTR-63). Ft. Collins, CO: U.S. Department of Agriculture, Forest Service, Rocky Mountain Research Station. <https://doi.org/10.2737/RMRS-GTR-63>
- Rolstad, C., Haug, T., & Denby, B. (2009). Spatially integrated geodetic glacier mass balance and its uncertainty based on geostatistical analysis: application to the western Svartisen ice cap, Norway. *Journal of Glaciology*, 55(192), 666–680. <https://doi.org/10.3189/002214309789470950>
- Sajedi-Hosseini, F., Choubin, B., Solaimani, K., Cerdà, A., & Kavian, A. (2017). Spatial prediction of soil erosion susceptibility using a fuzzy analytical network process: Application of the fuzzy decision making trial and evaluation laboratory approach. Retrieved from <https://onlinelibrary.wiley.com/doi/10.1002/ldr.3058>
- Shean, D. E., Alexandrov, O., Moratto, Z. M., Smith, B. E., Joughin, I. R., Porter, C., & Morin, P. (2016). An automated, open-source pipeline for mass production of digital elevation models (DEMs) from very-high-resolution commercial stereo satellite imagery. *ISPRS Journal of Photogrammetry and Remote Sensing*, 116, 101–117. <https://doi.org/10.1016/j.isprsjprs.2016.03.012>
- Westerling, A. L., Hidalgo, H. G., Cayan, D. R., & Swetnam, T. W. (2006). Warming and Earlier Spring Increase Western U.S. Forest Wildfire Activity. *Science*, 313(5789), 940–943. <https://doi.org/10.1126/science.1128834>
- Wheaton, J. M., Brasington, J., Darby, S. E., & Sear, D. A. (2009). Accounting for uncertainty in DEMs from repeat topographic surveys: improved sediment budgets. *Earth Surface Processes and Landforms*, n/a-n/a. <https://doi.org/10.1002/esp.1886>
- Yang, B., & Chen, C. (2015). Automatic registration of UAV-borne sequent images and LiDAR data. *ISPRS Journal of Photogrammetry and Remote Sensing*, 101, 262–274. <https://doi.org/10.1016/j.isprsjprs.2014.12.025>
- Yousefi, S., Pourghasemi, H. R., Avand, M., Janizadeh, S., Tavangar, S., & Santosh, M. (2021). Assessment of land degradation using machine-learning techniques: A case of declining rangelands. *Land Degradation & Development*, 32(3), 1452–1466. <https://doi.org/10.1002/ldr.3794>
- Zhu, B., Ye, Y., Zhou, L., Li, Z., & Yin, G. (2021). Robust registration of aerial images and LiDAR data using spatial constraints and Gabor structural features. *ISPRS Journal of Photogrammetry and Remote Sensing*, 181, 129–147. <https://doi.org/10.1016/j.isprsjprs.2021.09.010>